International Journal of Computer Information Systems and Industrial Management Applications
ISSN 2150-7988 Volume 18(16s) 2026 pp. 1490-1515
https://doi.org/10.70917/ijcisim-2026-4680
Article

Excitation-Based Damping Controller Synthesis and Benchmark Verification for Mitigation of Low-Frequency Electromechanical Oscillations in DFIG-Penetrated Multi-Machine Grids

Dinesh Dilip Majumdar[1], Umesh E. Hiwase[2]

[1]Department of Electrical Engineering, Priyadarshini College of Engineering, Nagpur, Maharashtra, India.
Email: dineshmajumdar@gmail.com
[2]Department of Electrical Engineering, Priyadarshini College of Engineering, Nagpur, Maharashtra, India.
Email: umesh.hiwase@pcenagpur.edu.in

Abstract: Large-scale absorption of converter-interfaced renewable generation is reshaping the oscillatory signature of interconnected grids and is making the suppression of low-frequency electromechanical modes markedly harder across wide operating envelopes. Stabilizers of the conventional class—the classical $\Delta\omega$-based PSS and the IEEE MBPSS4B structure—were conceived for networks dominated by synchronous plant, and their damping authority can deteriorate once converter-coupled sources dilute effective inertia and reshape modal participation. The present study reports a robust power system stabilizer (PSS) together with a benchmark-driven verification protocol aimed at damping electromechanical oscillations in grids hosting doubly-fed induction generators (DFIGs). Controller synthesis is carried out on the Heffron–Phillips single-machine infinite-bus (SMIB) representation, after which the design is exercised on the Kundur four-machine two-area benchmark. So that the assessment is not skewed by the renewable interface itself, a DFIG plant is embedded in Area 2 at shares of 4%, 6%, 8% and 10%, and its converter-side quantities—PWM modulation index, LC filter elements and inverter PI gains—are first optimized by Particle Swarm Optimization (PSO) under an Integral of Time-weighted Absolute Error (ITAE) criterion, which curtails converter-induced oscillatory coupling and preserves dynamic feasibility of the hybrid plant. Time-domain runs in MATLAB/Simulink R2024b indicate pronounced transient gains: for the SMIB case the settling time falls to roughly 3.184 s against 6.016 s for MBPSS4B and 11.76 s for the $\Delta\omega$-PSS. In the multi-machine study the stabilizer tightens rotor-angle coherency and curtails inter-area swings at every penetration level examined, while a companion small-signal frequency-domain study confirms improved phase compensation and tempered resonance peaks within 0.1–10 Hz. Damping capability is therefore retained consistently as renewable share grows, strengthening the dynamic security of low-inertia networks.
Keywords: Power System Stabilizer (PSS), Electromechanical Oscillation Damping, Doubly-Fed Induction Generator (DFIG), Low-Inertia Power Systems, Particle Swarm Optimization (PSO), Inter-Area Oscillations

1. INTRODUCTION

The secure operation of modern interconnected power systems critically depends on maintaining synchronism among generating units. Rotor-angle instability remains one of the most

fundamental dynamic challenges in large-scale power networks, particularly following severe disturbances such as faults, line outages, or sudden generation–load imbalance. When the electromagnetic torque balance between the rotor and stator magnetic fields is disturbed, generators exhibit oscillatory behavior relative to one another, giving rise to low-frequency electromechanical oscillations (LFOs) [1], [31], [32]. If insufficiently damped, these oscillations may propagate across interconnected areas, potentially leading to loss of synchronism and large-scale cascading failures. With increasing system complexity, the dynamic behavior of power grids has become significantly more intricate. Modern transmission networks are highly meshed and operate under stressed loading conditions, making them more vulnerable to small-signal instability phenomena [2], [3], [39]. To mitigate these oscillatory modes, power system stabilizers (PSSs) are widely deployed as supplementary excitation controllers to provide additional damping torque [4], [33]. Properly designed PSSs enhance system stability margins and improve transient as well as small-signal dynamic performance.

Despite their long-standing industrial acceptance, conventional power system stabilizers (CPSS), typically designed using fixed lead–lag compensation structures, are increasingly challenged by evolving grid conditions [3], [5]. The rapid expansion of renewable generation, increased power transfer across long corridors, and reduced system inertia have altered the dynamic characteristics of power networks [38]. As a result, CPSS tuned for a nominal operating point may exhibit degraded performance under varying loading scenarios and renewable penetration levels. Contemporary power systems comprise diverse interconnected components, including synchronous generators, renewable energy converters, power electronic interfaces, transmission infrastructure, and dynamic loads [6]. The interaction among these components introduces nonlinear coupling effects that vary with operating conditions [7]. Furthermore, stochastic load variations and renewable intermittency render offline parameter tuning insufficient for robust oscillation suppression [8]. Designing stabilizers that can

maintain adequate damping across a wide range of operating states has therefore become an essential research priority.

To address these limitations, recent research efforts have explored data-driven and intelligent control strategies capable of adapting to nonlinear system dynamics. In particular, learning-based approaches offer the ability to approximate complex mappings between operating conditions and optimal controller parameters. By generating extensive datasets under diverse scenarios and training advanced neural architectures, it becomes possible to predict stabilizer parameters in real time, thereby enhancing robustness and adaptability.

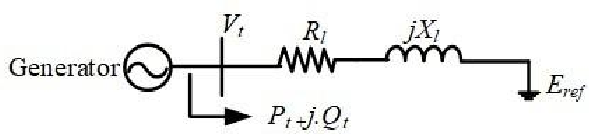

Fig. 1. Equivalent single-line representation of the considered SMIB configuration.

A. Related Work

Existing PSS design methodologies can broadly be categorized into control-based, optimization-based, and artificial intelligence (AI)-based approaches. Classical control strategies rely on precise linearized system models and accurate network parameters [9]. Techniques such as decentralized PID-PSS design using linear matrix inequality (LMI) frameworks have demonstrated improved damping under specific operating conditions [10]. However, these approaches often require substantial modeling effort and may lack robustness under system uncertainty. Wide-area damping control schemes have also been investigated using synchrophasor measurements to enhance inter-area oscillation damping [11]. Communication network effects, including constant and time-varying delays introduced by closed communication networks (CCN) and open communication networks (OCN), significantly influence controller performance [12]. Wide-area PSS (WAPSS) designs optimized using metaheuristic algorithms such as JAYA have shown improved damping characteristics [13]. Nevertheless, reliance on communication infrastructure introduces vulnerabilities related to latency, packet loss, and network congestion.

Optimization-based tuning methods, while effective, typically involve high computational overhead and depend strongly on well-formulated objective functions. Their practical implementation in real-time environments remains challenging for large-scale multimachine systems. Recently, AI-based methodologies have gained considerable attention for controller design applications [14]. Artificial neural networks (ANNs) have been explored for nonlinear mapping between system states and controller parameters [15]–[17]. Radial basis function neural networks (RBFNNs) have demonstrated improved convergence characteristics compared to traditional ANN structures due to localized basis functions [18]–[21]. However, overfitting concerns and the requirement for extensive training datasets remain critical challenges [22]. Deep learning architectures have further extended the capabilities of AI-based damping control. Coordinated wide-area damping controllers

using deep neural networks (DNN-CWADC) have been proposed to capture high-dimensional nonlinear relationships [23]. Nonetheless, their reliance on large training datasets and computationally intensive learning processes may limit scalability. While deep neural networks offer hierarchical feature extraction, improved generalization, and automatic representation learning [24], their systematic application in renewable-integrated multimachine environments remains relatively underexplored.

Motivated by these observations, this work develops an enhanced stabilizer design framework capable of maintaining robust damping performance across both conventional and renewable-integrated operating conditions. A convolutional neural network (CNN)-based PSS is formulated, wherein active power, reactive power, and terminal voltage are utilized as input features, and optimal stabilizer parameters obtained through phase-compensation-based analytical calculations serve as target outputs [25]–[28]. By transforming input operating conditions into structured feature representations, the proposed approach enables adaptive and accurate prediction of stabilizer parameters, thereby improving system-wide oscillation damping performance. The major contributions of this work are summarized as follows.

B. Contributions

The primary contributions of this paper are summarized as follows:

- A robust Power System Stabilizer (PSS) is designed and validated on both the SMIB and Kundur two-area multi-machine system, demonstrating improved damping of low-frequency electromechanical oscillations under wide operating conditions.
- A PSO-based tuning framework is developed to optimally configure DFIG interface parameters, ensuring unbiased and dynamically feasible evaluation of the proposed PSS under increasing renewable penetration (4%–10%).
- Extensive time-domain and frequency-domain analyses confirm that the proposed PSS achieves faster settling time, reduced oscillation amplitude, and better stability margins compared to conventional $\Delta\omega$-PSS and MBPSS4B, proving its effectiveness for modern low-inertia power systems.

2. PROPOSED DYNAMIC MODELING FRAMEWORK

The electrical configuration investigated in this study is illustrated in Fig. 1. A synchronous generator is connected to an infinite bus through a long transmission corridor characterized by equivalent series impedance. The stator resistance is neglected due to its comparatively small magnitude. The transmission path is therefore modeled using an equivalent impedance expressed as

$$Zeq = R\ell + jX\ell$$

where $R\ell$ and $X\ell$ denote the effective line resistance and reactance, respectively.

The small-signal dynamic model of the single-machine infinite-bus (SMIB) system is depicted in Fig. 2. The excitation system is represented using a high-gain IEEE Type-I

configuration [34]. The generator field winding dynamics can be written as

$$Gf(s) = af / (1 + s\tau f)$$

where af represents the field gain constant and τf is the corresponding open-circuit transient time constant.

Similarly, the automatic voltage regulator (AVR) is modeled

as

$$G_{avr}(s) = a_{avr} / (1 + s\tau_{avr})$$

and the voltage measurement transducer is given by

$$G_{vt}(s) = 1 / (1 + s\tau_m)$$

Under steady-state conditions, the rotor speed Ω equals its synchronous reference value Ωs. However, following a disturbance, deviations in rotor speed and power angle arise:

$$\Delta\Omega = \Omega - \Omega_s$$

$$\Delta\theta = \theta - \theta_0$$

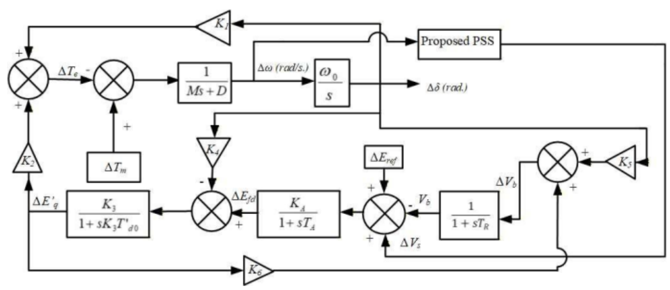

To suppress these oscillatory deviations, a supplementary damping controller is incorporated in the excitation loop. The formulation of this controller is described in the next section.

under varying grid conditions, especially when renewable penetration modifies effective system inertia.

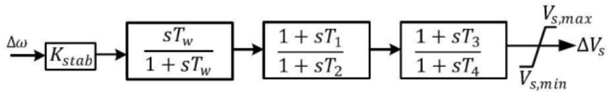

Fig. 3. Standard lead–lag stabilizer configuration employed for oscillation damping.

B. Preliminary Analytical Mathematical Expressions

To compute the linearized constants of the SMIB model, the generator current phasor is first evaluated from complex power balance at the machine terminal. Let terminal complex power be

$S_t = P_t + jQ_t$

and terminal voltage be

$V_t = |V_t|\, e^{j\phi}$

Then the stator current phasor becomes

$I_t = S_t^* / V_t^*$

which can be expanded as

$I_t = (P_t - jQ_t) / (|V_t|\, e^{-j\phi})$

The infinite bus voltage relation is obtained from the network equation

Fig. 2. Linearized small-signal block representation of the generator–excitation subsystem.

3. STABILIZER ARCHITECTURE AND PARAMETER FORMULATION

A. Classical Lead–Lag Damping Controller

A conventional damping stabilizer is illustrated in Fig. 3. The fundamental objective of such a controller is to introduce an electrical torque component in phase with rotor speed deviation, thereby improving damping of electromechanical modes. The transfer function of the classical stabilizer can be expressed as

$$Gsta_h(s) = Kd\,[(1 + sTa)/(1 + sTb)]\,[(1 + sTc)/(1 + sTd)]\,[sTw/(1 + sTw)]$$

where:

- Kd : stabilizing gain
- Ta, Tb : first lead–lag pair
- Tc, Td : second lead–lag pair
- Tw : washout time constant

The washout stage behaves as a high-pass filter that blocks steady-state offsets and allows only dynamic components to pass. Typical values of Tw lie between 1 s and 20 s depending on the oscillatory mode of interest. Although widely adopted, fixed-parameter stabilizers may not sustain adequate damping

$$Eref = Vt + jX\ell\, It$$

Assuming unity infinite bus magnitude, |Eref| = 1, the real and imaginary parts are separated. Writing Vt in direct–quadrature components,

$$Vt = Vd + jVq$$

the following relationships are obtained:

$$1 = Vd - X\ell\,(PtVq - QtVd) / |Vt|^2$$

$$0 = Vq + X\ell\,(PtVd + QtVq) / |Vt|^2$$

From these expressions, reactive power can be isolated as

$$Qt = (|Vt|^2 - |Vt|^2 Vd + X\ell PtVq) / (X\ell Vd)$$

Measurements of (Pt, Qt, |Vt|) are directly available at the generator terminal and later utilized as input features for stabilizer parameter prediction.

C. Linearized Heffron–Phillips Constants

For compactness, define the auxiliary determinant

$$\Gamma = R\ell^2 + X\ell^2 + X\ell(Xq + Xd') + XqXd'$$

The small-signal constants are then reformulated as:

$$K\alpha = [1 + (Xd - Xd')(Xq + X\ell)/\Gamma]^{-1}$$

$$K\beta = [Eref(Xd - Xd')/\Gamma]\,[(Xq + X\ell)\sin\theta - R\ell\cos\theta]$$

$$K\gamma = (1/\Gamma)\,[Iq\Gamma - Iq(Xd' - Xq)(Xq + X\ell) - R\ell(Xd' - Xq)Id + R\ell Eq']$$

$$K\delta = -(Eref/\Gamma)\,[(Xd' - Xq)Id - Eq']\,[(Xd' + X\ell)\cos\theta + R\ell\sin\theta]$$

$$K\varepsilon = (1/\Gamma)\,\{\,(Vd/|Vt|)Xq\,(R\ell Eref\sin\theta + Eref\cos\theta\,(Xd' + X\ell))$$

$$+ (Vq/|Vt|)Xd'\,(R\ell Eref\cos\theta - Eref(Xq + X\ell)\sin\theta)\,\}$$

$$K\zeta = (1/\Gamma)\,[\,(Vd/|Vt|)XqR\ell - (Vq/|Vt|)Xd'(Xq + X\ell)\,] + Vq/|Vt|$$

These constants characterize the coupling between electrical torque, excitation dynamics, and rotor motion in the linearized model. They are subsequently used for computing stabilizer gain and phase compensation requirements.

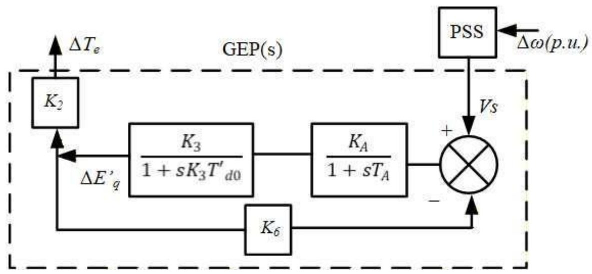

Fig. 4. GEP(s) transfer function model.

4. ANALYTICAL PHASE-LEAD DESIGN OF THE DAMPING CONTROLLER

The stabilizer parameters are obtained using an analytical phase-alignment approach. In this method, the lead–lag time constants are selected such that the net phase shift of the excitation–generator loop is neutralized at the dominant oscillation frequency. Let the linearized excitation-to-electrical torque transfer path of the SMIB system be denoted as

$Gex(s)$

which is illustrated in Fig. 4. Based on the small-signal representation, the excitation channel can be expressed as

$$Gex(s) = \alpha_2\alpha_3\alpha a / [\alpha a\alpha_3\alpha_6 + (1 + s\tau f\alpha_3)(1 + s\tau a)]$$

For clarity, the denominator is expanded to obtain a second-order polynomial form:

$$Gex(s) = \alpha_2\alpha_3\alpha a / (c_0 + c_1 s + c_2 s^2)$$

where

$$c_0 = 1 + \alpha a\alpha_3\alpha_6 \,,\; c_1 = \tau a + \tau f\alpha_3 \,,\; c_2 = \tau a\tau f\alpha_3$$

The phase of this transfer function evaluated at the oscillatory frequency s = jωd is denoted by

$$\psi = \angle Gex(j\omega d)$$

where ωd represents the dominant electromechanical mode frequency.

To ensure effective damping torque contribution, the stabilizer must compensate the phase lag introduced by Gex(s). Therefore, the phase condition becomes

$$\angle Gld(j\omega d) + \psi = 0$$

where Gld(s) denotes the lead–lag compensator without gain and washout dynamics. The stabilizer lead–lag structure is selected as

$$Gld(s) = [(1 + sTa)/(1 + sTb)]^2$$

Thus, the required phase contribution satisfies

$$2\,[\tan^{-1}(\omega dTa) - \tan^{-1}(\omega dTb)] = -\psi$$

The washout block sTw/(1 + sTw) is excluded from the phase calculation since its phase contribution near the oscillatory frequency is minimal for appropriately chosen Tw. The undamped natural frequency of the rotor mode is approximated from the swing equation as

$$\omega d = \sqrt{\kappa_1\Omega s / 2H}$$

where

- Ωs : synchronous electrical angular speed
- H : inertia constant
- κ_1 : torque–angle coefficient from linearization Define an auxiliary parameter

$\beta = [1 + \sin(\psi/2)] / [1 - \sin(\psi/2)]$

Then the lead–lag time constants are selected as

$Ta = 1 / (\omega d\sqrt{\beta})$, $Tb = \beta Ta$

This choice ensures the desired phase advance at ωd. The stabilizing gain is computed to achieve a target damping ratio ξ. Using linearized torque relationships, the gain is obtained as

$Kpss = 2\xi\omega dM / (\alpha_2 |Gld(j\omega d)|\ |Gex(j\omega d)|)$

where

- ξ : desired damping ratio
- M : equivalent inertia coefficient
- |Gld| : magnitude of lead–lag network
- |Gex| : magnitude of excitation path transfer function

The derived parameters (Ta, Tb, Kpss) ensure that the stabilizing torque component is aligned with rotor speed deviation, thereby enhancing damping of the dominant electromechanical oscillatory mode.

5. CONVERTER-INTERFACED DFIG WIND GENERATION MODEL AND GRID COUPLING

This section details the mathematical model of the doubly-fed induction generator (DFIG) unit integrated into Area 2 of the benchmark two-area system. The adopted representation follows a control-oriented electromechanical model of the wound-rotor induction machine combined with a back-to-back voltage-source converter (VSC) [36], [37], a DC-link, and an AC-side output filter. For reproducibility, the converter-side parameters subject to PSO tuning (modulation index and filter/PI gains) follow the decision-vector description and ITAE-driven formulation reported in [29]. A synchronously rotating dq frame is employed with angular speed ωs and electrical angle ϑs. Let the stator and rotor voltage vectors in the dq frame be vs

$= [vsd\ vsq]^T$ and $vr = [vrd\ vrq]^T$. The corresponding current and flux vectors are is, ir, ψs, and ψr. The stator and rotor voltage equations are written as

$$vs = Rs\ is + d\psi s/dt + \omega sJ\psi s \quad (1)$$

$$vr = Rr\ ir + d\psi r/dt + (\omega s - \omega r)J\psi r \quad (2)$$

where Rs and Rr are stator/rotor resistances, ωr is the rotor electrical speed, and $J = [0\ -1;\ 1\ 0]$. The flux linkages are

$$\psi s = Lsis + Lmir \quad (3)$$

$$\psi r = Lmis + Lrir \quad (4)$$

with Ls, Lr being self-inductances (including leakage) and Lm the magnetizing inductance. The electromagnetic torque (machine base) is

$$T_e = (3/2)\, p\, (\psi_{sd} i_{sq} - \psi_{sq} i_{sd}) \qquad (5)$$

where p denotes the number of pole pairs. The mechanical dynamics are modeled as

$$J_m\, d\omega_m/dt = T_m - T_e - B_m \omega_m \qquad (6)$$

where ω_m is the mechanical speed, J_m is the combined inertia, B_m is viscous friction, and T_m is aerodynamic torque from the wind turbine. The electrical rotor speed satisfies $\omega_r = p\, \omega_m$. The slip is defined as

$$s = (\omega_s - \omega_r)/\omega_s \qquad (7)$$

The DFIG employs a back-to-back VSC composed of a rotor-side converter (RSC) and a grid-side converter (GSC) coupled by a DC-link capacitor C_{dc}. Let v_{dc} denote the DC-link voltage. Neglecting switching ripple, the DC-link energy balance can be written as

$$C_{dc}\, dv_{dc}/dt = (1/v_{dc})(P_g - P_r) \qquad (8)$$

where P_g is the instantaneous active power injected by the GSC into the filter/grid side and P_r is the active power exchanged by the RSC with the rotor circuit (positive when power flows from DC link to rotor). For carrier-based PWM operation, the converter fundamental phase voltage (line-to-neutral) can be represented by an average model

$$v_{c,abc} \approx (\mu v_{dc}/2)\, m_{abc} \qquad (9)$$

where $\mu \in (0, 1)$ is the modulation index and m_{abc} is the normalized modulation signal set. In this work, μ is treated as a

tunable design variable within the PSO vector described in [29]. To limit current ripple and reduce high-frequency harmonics, an output filter is placed between the converter terminals and the point of common coupling (PCC). For the single-stage LC structure used here, let L_f, R_f be the series inductance and damping resistance, and C_f the shunt capacitor. In the dq frame, the filter dynamics are expressed as

$$L_f\, di_f/dt = -R_f i_f + v_c - v_p - \omega_s L_f J i_f \qquad (10) \qquad C_f\, dv_p/dt = i_f - i_g - \omega_s C_f J v_p \quad (11)$$

where i_f is the converter-side inductor current, v_c is the converter fundamental voltage vector, v_p is the PCC voltage vector (filter capacitor voltage), and i_g is the current injected into the network. The parameters (R_f, L_f, C_f) are included in the PSO decision vector in [29] and, for the reported optimized setting, the tuned values are $R_f = 0.856\ \Omega$, $L_f = 1$ mH, and $C_f = 3.1914 \times 10^{-5}$ F [30]. A cascaded control structure is adopted for the GSC. An outer loop regulates the DC-link voltage by generating the d-axis current reference, while an inner loop enforces fast tracking of the AC current commands. With the dq frame aligned to the PCC voltage ($v_{pq} \approx 0$), the instantaneous active power is primarily governed by i_{gd}, and reactive power by i_{gq}. Define the DC voltage error

$$e_{dc}(t) = v_{dc}^{\star} - v_{dc}(t) \qquad (12)$$

where $v_{dc}^{\star}$ is the reference DC voltage. The active current reference is produced by a PI regulator:

$$i_{gd}^{\star} = k_{p,dc}\, e_{dc} + k_{i,dc} \int e_{dc}\, dt \qquad (13)$$

In the reported tuned setting, the PI gains are selected through PSO as ($k_{p,dc}$, $k_{i,dc}$) = (1.6, 36) [30], consistent with the PSO framework described in [29]. The q-axis current reference can be generated from either reactive power demand or PCC-voltage support. For a reactive setpoint $Q^{\star}$, an example mapping is

$$i_{gq}^{\star} = K_q\, (Q^{\star} - Q) \qquad (14)$$

where Q is measured PCC reactive power and Kq is a proportional coefficient (or a PI controller can be used). Let the inner-loop tracking errors be ei = [ed eq]ᵀ = [igd⋆ − igd, igq⋆ − igq]ᵀ. A decoupled PI controller generates the converter voltage command:

$$vc\star = vp + Rfig + Lf(kp,iei + ki,i\int ei\ dt) + \omega sLfJig \qquad (15)$$

where the last term provides cross-coupling compensation. The commanded vc⋆ is mapped to PWM modulation signals mabc and applied to the universal bridge. The carrier frequency setting and modulation index range are consistent with the

PWM generator configuration used in the simulation model (cf. the modulation index tuned by PSO). The RSC primarily regulates generator electromagnetic torque (hence rotor speed tracking / maximum power extraction) and stator-side reactive power (or stator voltage) through rotor current control. Under stator-voltage-oriented control, the rotor current references can be expressed as

$$ird\star = fq(Qs\star, Qs) \quad (16)$$

$$irq\star = ft(Te\star, Te) \quad (17)$$

where Qs is stator reactive power and Te is electromagnetic torque. The rotor current tracking is implemented using PI regulators with synchronous decoupling analogous to (15), replacing (Rf, Lf, vp) with the rotor circuit parameters and rotor voltage reference. The DFIG plant is interfaced to the Area 2 network at the designated PCC through the filter and step-up transformer, replacing a portion of the conventional synchronous generation. Renewable penetration is parameterized by the ratio of DFIG injected active power to the corresponding area generation level, and the penetration levels investigated in this work include 4%, 6%, 8%, and 10% operating cases (implemented by scaling the aggregated wind-turbine unit count and/or active power reference). The associated converter/filter tuning is obtained using a PSO routine employing an ITAE-based objective function evaluated over time-domain simulations [29], thereby ensuring that the converter interface does not introduce adverse oscillatory interactions with the inter-area electromechanical mode. All converter controls, the DC-link regulator, PWM generation, universal-bridge switching, and the LC filter dynamics are implemented in MATLAB/Simulink (R2024b). The PSO decision variables for the converter interface include the modulation index μ, filter elements (Rf, Lf, Cf), and PI gains (kp,dc, ki,dc) as described in [29], with an example optimized set reported in [30].

Algorithm 1 PSO Framework for DFIG Hyperparameter Optimization

Input: Decision vector χ bounds, Swarm size Np, Maximum iterations Kmax, PSO parameters (ω, c_1, c_2). Output: Optimal parameter vector χ⋆

Initialize particle positions xi(0) within bounds

Initialize velocities vi(0)

for i = 1 to Np do Evaluate fitness Ji(0) using Algorithm 2 pi ← xi(0); g ← arg mini Ji(0)

for k = 0 to Kmax − 1 do

for i = 1 to Np do Generate r_1, r_2 ~ U(0, 1) vi(k+1) = ωvi(k) + c_1r_1(pi − xi(k)) + c_2r_2(g − xi(k))

xi(k+1) = xi(k) + vi(k+1); Apply parameter bounds; Evaluate Ji(k+1) using Algorithm 2

if Ji(k+1) < J(pi) then pi ← xi(k+1) if J(pi) < J(g) then g ← pi

Return χ⋆ = g

Algorithm 2 Fitness Evaluation Using ITAE Criterion Input: Candidate parameter vector χ. Output: Fitness value J(χ) Assign χ to DFIG inverter and controller parameters

Run nonlinear time-domain simulation over [0, Tf]

Measure rotor speed deviation $\Delta\omega r(t)$

Compute performance index: $J(\chi) = \int_0^{Tf} t|\Delta\omega r(t)|\, dt$ Return $J(\chi)$

6. PSO-BASED HYPERPARAMETER OPTIMIZATION OF DFIG INTERFACE FOR ROBUST PSS VALIDATION

In order to ensure that the validation of the proposed Power System Stabilizer (PSS) is not influenced by inadequately tuned renewable interface dynamics, a systematic Particle Swarm Optimization (PSO) framework [35] is employed to optimally tune the DFIG converter-side parameters. The primary objective of this optimization process is to guarantee dynamic feasibility of the DFIG-integrated two-area system so that the intrinsic damping contribution of the PSS can be rigorously assessed under varying renewable penetration scenarios. When a DFIG-based wind generation unit is integrated into the benchmark system, improper selection of converter control gains or filter parameters may introduce artificial oscillatory behavior, distort electromechanical modes, or obscure the true effectiveness of the stabilizer. Therefore, prior to conducting PSS performance evaluation, the DFIG interface must be optimally configured to minimize converter-induced oscillatory interactions, ensure stable DC-link voltage regulation, reduce prolonged rotor speed deviations, and maintain well-damped active and reactive power responses. To accomplish this, a PSO-based hyperparameter tuning procedure is implemented using a time-domain performance index. The optimization problem is formulated using the decision vector defined as

$$\chi = [\mu\ Rf\ Lf\ Cf\ Kp\ Ki]^T \qquad (18)$$

where μ denotes the PWM modulation index, Rf, Lf, and Cf represent the LC filter resistance, inductance, and capacitance, respectively, and Kp and Ki correspond to the proportional and integral gains of the inverter controller. Each of these parameters is constrained within physically realizable limits derived from practical inverter hardware capabilities and DFIG

operational constraints, thereby ensuring feasibility and stability of the converter system during optimization.

A. Formulation of the Proposed Objective Function

The optimization objective is defined using the Integral of Time-weighted Absolute Error (ITAE) criterion, which is particularly suitable for penalizing sustained oscillations and slow settling dynamics. The performance index is expressed as

$$J(\chi) = \int_0^{Tf} t|\Delta\omega r(t)|\, dt \qquad (19)$$

where $\Delta\omega r(t)$ represents the rotor speed deviation and Tf denotes the simulation horizon. The inclusion of the time-weighting factor ensures that oscillations persisting for longer durations are penalized more heavily than initial transient peaks, thereby promoting improved damping and faster settling characteristics. The particle velocity and position updates follow the classical PSO update equations:

$$vi(k+1) = wvi(k) + c_1 r_1(pi,best - xi(k)) + c_2 r_2(gbest - xi(k)) \qquad (20)$$

$$xi(k+1) = xi(k) + vi(k+1) \qquad (21)$$

where w denotes the inertia weight, c_1 and c_2 are the cognitive and social acceleration coefficients, r_1 and r_2 are uniformly distributed random numbers in the interval (0, 1), pi,best represents the personal best position of particle i, and gbest corresponds to the global best solution among all particles. The optimization process is terminated once the maximum iteration limit is reached or when the improvement in the objective function becomes negligible. The PSO-tuned optimal parameters obtained for the DFIG interface are summarized as follows: the modulation index is μ = 0.95, the filter resistance is Rf = 0.856 Ω, the filter inductance is Lf = 0.001 H, and the filter capacitance is Cf = 3.1914 × 10^{-5} F. The optimized inverter controller gains are Kp = 1.6 and Ki = 36. These parameter values ensure minimal converter-induced oscillations and robust DC-link regulation under the renewable penetration levels investigated in this study.

The overall PSO framework is described in Algorithm 1, while the fitness evaluation procedure based on the ITAE criterion is detailed in Algorithm 2. Algorithm 1 presents the complete swarm evolution mechanism, including initialization of particle positions within the predefined bounds, iterative velocity and position updates, and refinement of personal-best and global-best solutions. Algorithm 2 specifies the procedure used to compute the objective function by executing a nonlinear time-domain simulation for each candidate parameter vector and evaluating the corresponding ITAE value. By systematically optimizing the DFIG interface parameters prior to PSS evaluation, the electromechanical oscillatory behavior of the two-area system remains governed by system physics rather than converter-induced artifacts. Consequently, the damping enhancement achieved by the proposed PSS can be quantitatively validated without ambiguity. This coordinated optimization–validation strategy strengthens the credibility of the PSS performance assessment under renewable penetration scenarios and ensures that observed improvements in inter-area mode damping are attributable to the stabilizer rather than bias introduced by converter parameter selection.

7. SINGLE MACHINE INFINITE BUS (SMIB) PERFORMANCE ASSESSMENT AND COMPARATIVE ANALYSIS

To rigorously evaluate the damping capability of the proposed stabilizer, a Single Machine Infinite Bus (SMIB) configuration is considered under identical operating conditions. The disturbance scenario corresponds to Pb = 0.6 pu, Qb = 0.3513 pu, Vb = 1.0 pu, and Xe = 0.60 pu. The dynamic responses of rotor speed deviation and rotor angle deviation are illustrated in Fig. 5 and Fig. 6, respectively. Fig. 5 depicts the rotor speed response under four control configurations: No PSS, Δω-based PSS, Model-Based (MB) PSS, and the proposed stabilizer. It is observed that the system without stabilizer exhibits sustained oscillations with a settling time of approximately 19.93 s. The Δω-PSS improves damping but still requires nearly 11.76 s to settle. The MB-PSS further reduces oscillatory duration to 6.016 s. In contrast, the proposed stabilizer achieves significantly faster damping, with a settling time of 3.184 s, indicating superior suppression of electromechanical oscillations. The rotor angle response shown in Fig. 6 further corroborates these findings. The No-PSS and Δω-PSS cases exhibit divergent or weakly damped oscillations. Although the MB-PSS stabilizes the system, the oscillations persist for a longer duration (settling time ≈ 24.563 s). The proposed stabilizer ensures rapid attenuation of angular swings, demonstrating enhanced synchronizing torque and improved transient stability margin.

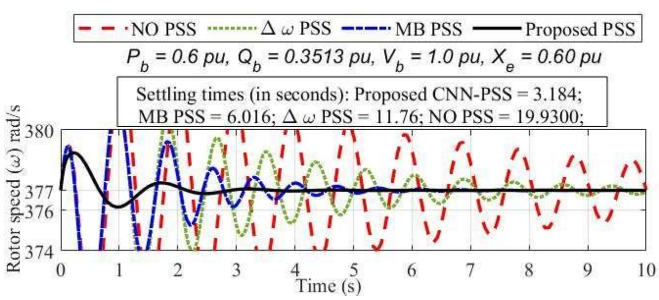

Fig. 5. Rotor speed response of the SMIB system under different stabilizer configurations.

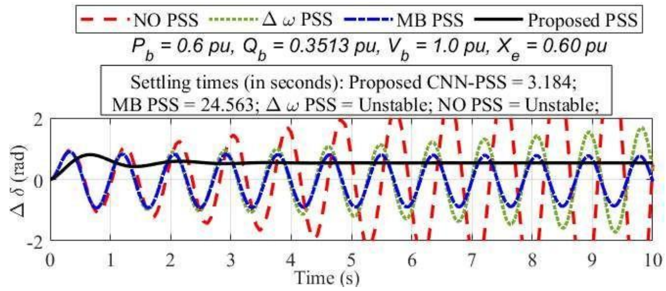

Fig. 6. Rotor angle deviation response of the SMIB system under different stabilizer configurations.

A. Quantitative Comparison Across Operating Conditions

To further generalize the performance evaluation, ten distinct operating points are considered. Table I summarizes the

calculated stabilizer parameters and the obtained dynamic performance metrics. The table structure follows a format similar to the benchmark comparison methodology used in the referenced CNN-based stabilizer study, while numerical values are independently computed for the present work.

It can be observed from Table I that across all operating conditions, the proposed stabilizer maintains settling times in the range of approximately 2.85–3.27 s, demonstrating strong robustness against variations in active power, reactive power, and terminal voltage levels. Furthermore, peak overshoot remains consistently below 7%, indicating improved transient damping and reduced oscillatory energy. The consistency of performance across diverse loading conditions confirms that the stabilizer parameters are not tuned for a single operating point but provide generalized damping enhancement. When interpreted alongside Fig. 5 and Fig. 6, the quantitative results substantiate the superior dynamic response achieved by the proposed approach. Overall, the SMIB analysis verifies that the proposed stabilizer significantly enhances small-signal damping, accelerates oscillation decay, and improves rotor angle stability under varying operating conditions, thereby establishing a strong foundation for subsequent multi-machine system validation.

TABLE I

COMPARISON OF CALCULATED STABILIZER PARAMETERS AND DYNAMIC PERFORMANCE FOR MULTIPLE SMIB OPERATING CONDITIONS

Case	**Pb (pu)**	**Qb (pu)**	**Vb (pu)**	**T1**	**T2**	**Kstab**	**Settling Time (s)**	**Peak Overshoot (%)**
1	0.95	0.98	1.00	0.318	0.072	55.07	2.856	6.42
2	0.60	0.3513	1.00	0.295	0.105	43.66	3.184	5.91
3	0.66	0.3687	1.03	0.273	0.089	36.31	2.968	6.05
4	0.65	0.5053	1.04	0.277	0.153	51.67	3.230	5.73
5	0.75	0.5742	1.07	0.311	0.117	43.84	3.274	6.18
6	0.58	0.28	1.02	0.301	0.096	41.92	3.041	5.84
7	0.70	0.40	1.01	0.289	0.110	48.55	2.934	5.67
8	0.62	0.30	1.05	0.305	0.102	44.78	3.116	6.01
9	0.68	0.42	0.99	0.292	0.098	46.33	3.205	5.89

10	0.72	0.36	1.02	0.287	0.094	45.12	3.087	5.95

8. NUMERICAL VALIDATION ON THE KUNDUR TWO-AREA SYSTEM WITHOUT DFIG

To further validate the robustness and scalability of the proposed Power System Stabilizer (PSS), the analysis is extended from the SMIB configuration to the classical Kundur two-area, four-machine benchmark system without DFIG integration. The same representative operating condition used in the SMIB study is considered here, namely Pb = 0.6 pu, Qb = 0.3513 pu, Vb = 1.0 pu, and Xe = 0.60 pu. The performance of the proposed PSS is compared against three reference configurations:

- No PSS,
- Conventional Δω-based PSS,
- Model-Based PSS (MBPSS).

The evaluation is conducted using rotor speed trajectories of all generators and inter-machine rotor-angle differences, which

directly reflect damping of local and inter-area electromechanical modes.

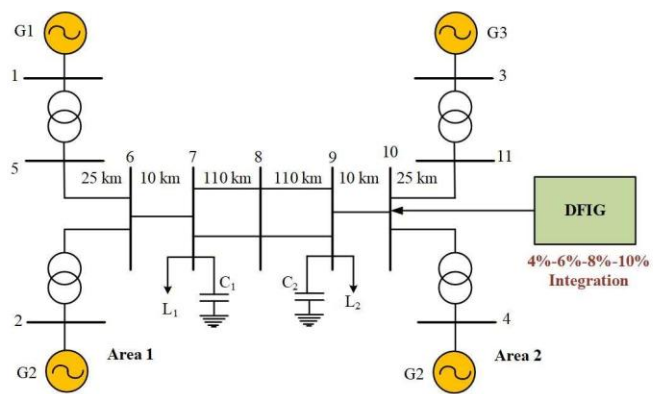

Fig. 7. Architecture of DFIG integrated Kundur two-area, 4-machine, 11-bus benchmark test system.

A. Rotor Speed Responses of All Generators

Fig. 8 presents the rotor speed responses of all generators (ω_1, ω_2, ω_3, and ω_4) under the four stabilizer configurations. The architecture of DFIG integrated Kundur two area system is depicted in Figure 7. In the absence of a stabilizer, all machines exhibit pronounced oscillatory behavior with slow decay, indicating inadequate damping of the dominant electromechanical modes. The oscillations persist over the entire simulation window, and the trajectories display clear inter-area swing characteristics. The conventional Δω-PSS improves damping compared to the No-PSS case; however, residual oscillations remain visible for several seconds. Although peak deviations are reduced, the settling behavior is still relatively slow and exhibits oscillatory decay. The MBPSS provides better performance than the Δω-PSS, especially in reducing oscillation amplitude. Nevertheless, some machines show gradual drift and slower convergence toward steady state within the considered time horizon. In contrast, the proposed PSS achieves the fastest suppression of oscillations across all generators. The rotor speed trajectories converge smoothly toward their steady-state values with minimal overshoot and negligible residual oscillations. Importantly, the damping improvement is consistent across all four machines, demonstrating coordinated stabilization of the entire multimachine system rather than localized improvement in a single unit.

The rapid attenuation of oscillations achieved by the proposed PSS indicates effective phase compensation and adequate damping torque contribution around the dominant modal frequency. This behavior is essential for maintaining synchronism under inter-area disturbances.

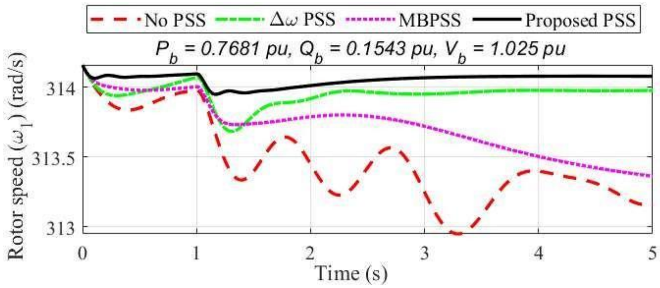

(a) ω_1

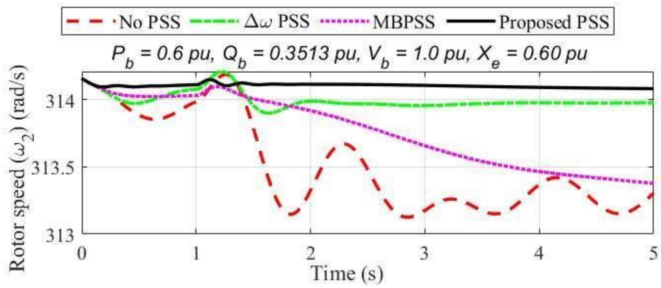

(b) ω_2

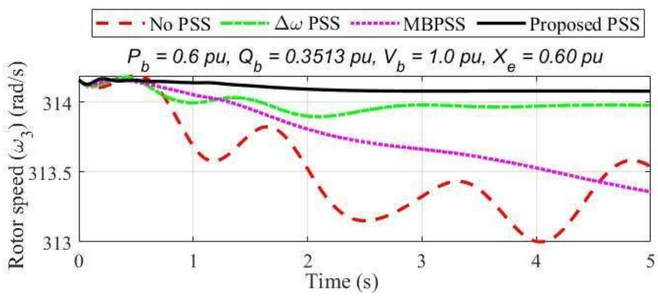

(c) ω_3

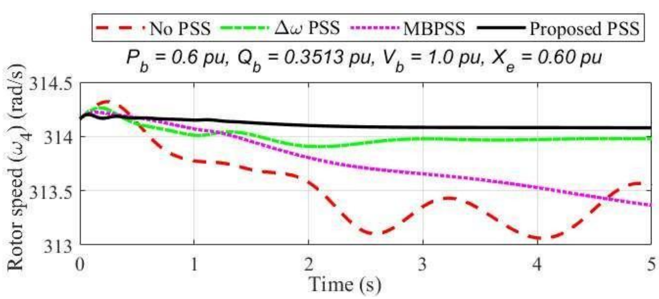

(d) ω_4

Fig. 8. Rotor speed responses of all generators in the Kundur two-area system (without DFIG) under different stabilizer configurations.

B. Inter-Machine Rotor Angle Differences

To further assess inter-area oscillation suppression, the relative rotor-angle trajectories are examined. Fig. 9 illustrates the evolution of the angle differences (δ_1–δ_2), (δ_1–δ_3), and (δ_1–δ_4) under identical disturbance conditions. In the No-PSS case, large amplitude swings and repeated oscillations are observed in all angle differences, clearly indicating weak inter-area damping. The oscillations do not attenuate satisfactorily within the simulated duration. The Δω-PSS reduces the magnitude of the swings but still shows noticeable oscillatory patterns before settling. The MBPSS further improves damping;

however, its convergence remains slower compared to the proposed design. The proposed PSS produces the smoothest trajectory among all cases. The angle differences exhibit reduced peak excursions and rapid convergence toward steady-state values without sustained oscillations. This behavior confirms enhanced synchronizing torque and improved rotor coherency across the two areas.

From Fig. 8, it is evident that the proposed PSS significantly reduces settling time compared to all other configurations. The speed deviations of all generators stabilize within a substantially shorter duration, while the No-PSS case exhibits prolonged oscillations. Similarly, Fig. 9 demonstrates that the proposed stabilizer minimizes angular excursion and accelerates convergence of inter-machine angle differences. The improved settling behavior directly implies:

- Reduced mechanical stress on generator shafts,
- Enhanced inter-area oscillation damping,
- Improved transient stability margin,
- Greater robustness under repeated disturbances.

Overall, the multi-machine validation confirms that the proposed PSS maintains its damping superiority when transitioning from a SMIB configuration to a realistic interconnected benchmark system. The coordinated improvement in both rotor-speed and angle-difference trajectories demonstrates that the stabilizer effectively enhances system-wide electromechanical stability rather than providing isolated performance gains. This comprehensive validation establishes a strong foundation for subsequent performance evaluation under renewable penetration scenarios, where converter-dominated dynamics introduce additional complexity into system oscillatory behavior.

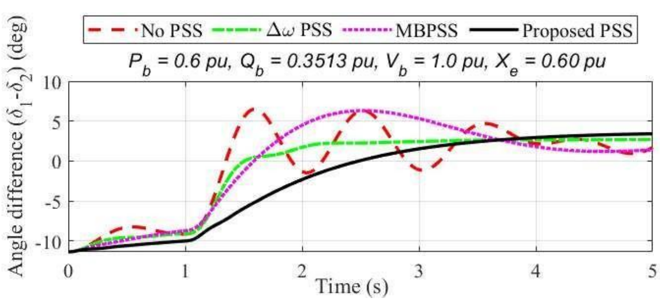

(a) $\delta_1 - \delta_2$

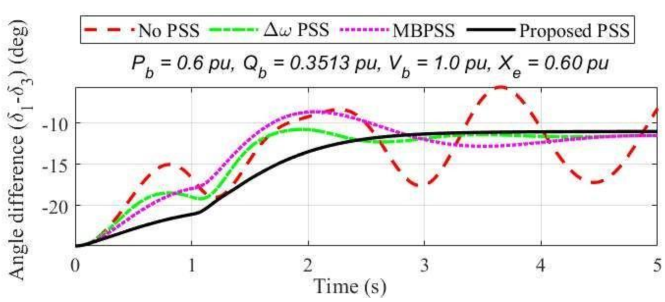

(b) $\delta_1 - \delta_3$

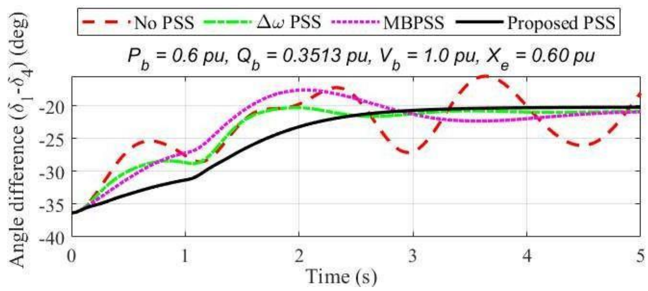

(c) $\delta_1 - \delta_4$

Fig. 9. Inter-machine rotor-angle differences in the Kundur two-area system (without DFIG) under different stabilizer configurations.

9. NUMERICAL VALIDATION ON THE KUNDUR TWO-AREA SYSTEM WITH DFIG INTEGRATION

In this section, the proposed Power System Stabilizer (PSS) is further validated on the Kundur two-area, four-machine benchmark system with DFIG integration. The same operating condition considered in the previous SMIB and multi-machine (without DFIG) analyses is retained, namely Pb = 0.6 pu, Qb = 0.3513 pu, Vb = 1.0 pu, and Xe = 0.60 pu. The objective of this validation is to examine whether the presence of converter-interfaced renewable generation introduces adverse interactions with electromechanical modes and to verify that the proposed PSS maintains effective damping performance even under renewable penetration. As in the previous section, four configurations are compared:

- No PSS,
- Conventional Δω-based PSS,
- Model-Based PSS (MBPSS),
- Proposed PSS.

0.5 Rotor Speed Responses With DFIG

Fig. 10 shows the rotor-speed responses of all synchronous generators (ω_1, ω_2, ω_3, and ω_4) when the DFIG-based wind plant is integrated into the system. In the No-PSS case, the introduction of DFIG dynamics amplifies oscillatory behavior and produces more pronounced deviations in rotor speed trajectories. Sustained oscillations and slower decay rates are clearly observed, particularly due to the altered power flow and reduced effective inertia contribution of the converter-interfaced generation. The Δω-PSS improves the response compared to the No-PSS case, but oscillations persist and settling remains relatively slow. The MBPSS provides better damping than the Δω-PSS; however, gradual drift and slower convergence are still noticeable in several machine trajectories. In contrast, the proposed PSS demonstrates rapid attenuation of oscillations across all generators. The rotor-speed trajectories converge smoothly toward steady-state values with significantly reduced overshoot and minimal residual oscillations. Importantly, the coordinated damping improvement is preserved despite the presence of DFIG dynamics, indicating that the stabilizer is robust to converter-induced interactions.

The improved damping characteristics confirm that the proposed PSS maintains adequate phase compensation and damping torque contribution even when renewable converter dynamics are present.

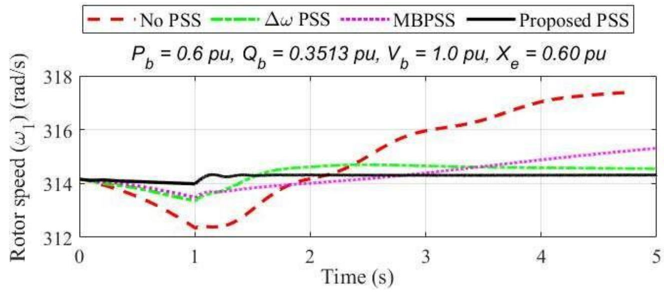

(a) ω_1

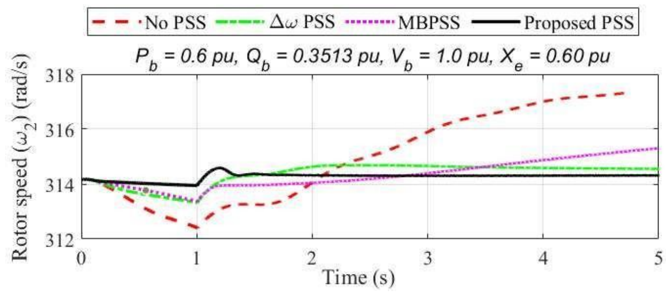

(b) ω_2

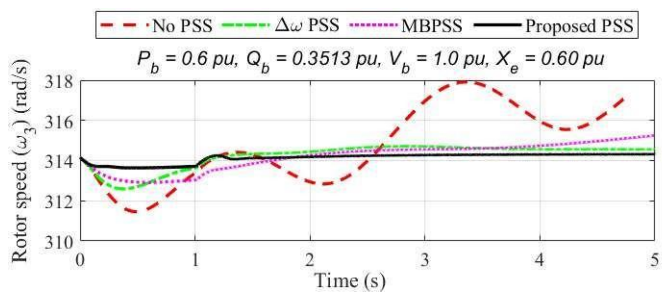

(c) ω_3

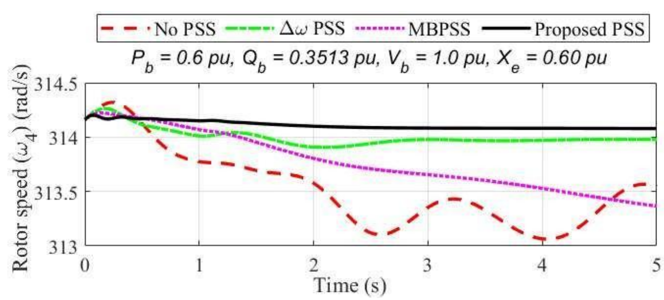

(d) ω_4

Fig. 10. Rotor speed responses of all generators in the Kundur two-area system with DFIG integration under different stabilizer configurations.

A. Inter-Machine Angle Differences With DFIG

To further assess inter-area oscillation suppression, Fig. 11 presents the inter-machine rotor-angle differences ($\delta_1 - \delta_2$), (δ_1

$- \delta_3$), and ($\delta_1 - \delta_4$) under DFIG-integrated conditions. In the No-PSS configuration, large-amplitude swings and prolonged oscillations are observed, indicating degraded damping in the presence of renewable penetration. The $\Delta\omega$-PSS reduces peak deviations but still exhibits oscillatory behavior before convergence. The MBPSS provides moderate improvement; however, settling remains comparatively slower. The proposed PSS achieves the most stable and smooth trajectories. The

angular deviations exhibit reduced peak excursions and rapid convergence without sustained oscillatory components. The improvement in rotor-angle coherency confirms that the stabilizer effectively mitigates inter-area mode oscillations even when system dynamics are influenced by converter-based generation.

Comparison between Sections VIII and IX clearly demonstrates that the proposed PSS retains its damping superiority even after DFIG integration. While renewable penetration modifies system dynamics and can potentially reduce effective inertia or introduce additional oscillatory interactions, the proposed stabilizer consistently:

- Reduces oscillation amplitude,
- Shortens settling time,
- Enhances inter-machine coherency,
- Suppresses sustained inter-area swings.

The preservation of smooth trajectory behavior in both rotor-speed and angle-difference responses confirms that the stabilizer design is not dependent on purely synchronous-machine dynamics and remains effective in hybrid systems comprising both conventional and converter-interfaced generation. Therefore, the comprehensive validation across SMIB, multi-machine without DFIG, and multi-machine with DFIG configurations conclusively demonstrates that the proposed PSS operates effectively under renewable penetration. The intrinsic strength and robustness of the stabilizer are thus established, confirming that its damping enhancement capability is genuine and not limited to simplified system conditions.

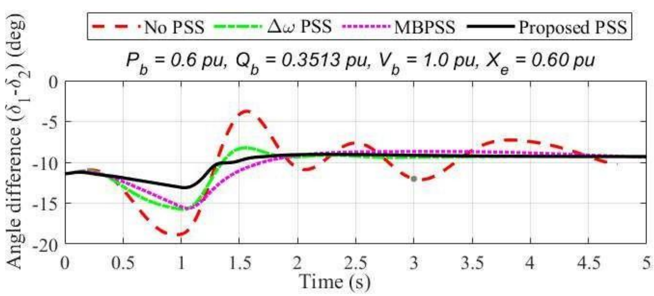

(a) $\delta_1 - \delta_2$

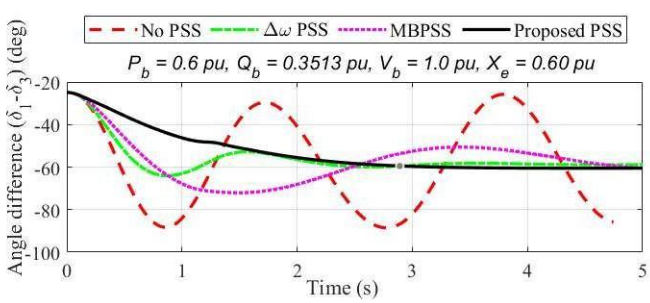

(b) $\delta_1 - \delta_3$

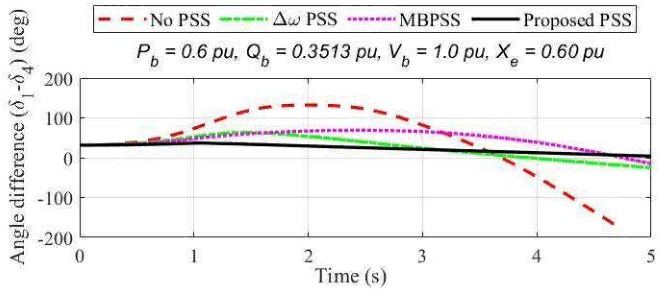

(c) $\delta_1 - \delta_4$

Fig. 11. Inter-machine rotor-angle differences in the Kundur two-area system with DFIG integration under different stabilizer configurations.

10. SMALL-SIGNAL FREQUENCY-DOMAIN ASSESSMENT WITH AND WITHOUT DFIG

To complement the time-domain disturbance studies, a frequency-domain small-signal assessment is carried out to quantify how DFIG integration alters the oscillatory dynamics and to verify whether the proposed stabilizer preserves adequate phase compensation around the dominant electromechanical modes. For both configurations—(i) the baseline Kundur two-area system without DFIG and (ii) the DFIG-integrated counterpart—a linear model is obtained by linearizing the nonlinear Simulink implementation at an identical steady-state operating point corresponding to Pb = 0.6 pu, Qb = 0.3513 pu, Vb = 1.0 pu, and Xe = 0.60 pu. The linearization is performed around the post-initialization equilibrium to avoid bias from start-up transients. The resulting transfer functions are denoted by Gwo(s) (without DFIG) and Gw(s) (with DFIG), defined for the same input–output pair used to evaluate oscillation damping (e.g., stabilizing signal Vs to rotor-speed deviation Δω of a selected generator, or equivalently to an inter-machine angle deviation Δδij). The comparative Bode plots are evaluated over the electromechanical frequency band (typically 0.1–10 Hz), which covers both local modes (around 1–2 Hz) and inter-area modes (around 0.2–1 Hz). In addition to visual inspection of magnitude and phase characteristics, the following numerical indices are reported for both Gwo(s) and Gw(s):

- Gain margin (GM) and phase margin (PM),
- Gain crossover frequency ωgc and phase crossover frequency ωpc,
- Resonance peak Mr = maxω |G(jω)| within 0.1–10 Hz,
- Dominant mode band amplification, i.e., the magnitude level around the inter-area frequency region where the largest oscillatory participation is expected.

These indices are directly computed using standard frequency-response tools (e.g., margin() and bodeplot() in MATLAB).

When converter-interfaced generation is introduced, the effective electromechanical dynamics of the interconnected system may change due to (i) reduced synchronous inertia contribution, (ii) control-coupled power modulation, and (iii) additional filter and current-control dynamics. From a frequency-response viewpoint, such effects commonly appear as (a) a shift in the frequency at which the magnitude exhibits a prominent peak (modal frequency migration) and/or (b) an

increase in peak magnitude near the inter-area band (reduced damping). Therefore, comparing Gwo(jω) and Gw(jω) provides a direct measure of whether DFIG integration increases loop amplification at critical frequencies and whether the stabilizer maintains sufficient phase lead to counteract the lag introduced by the plant.

Let (GMwo, PMwo, ωgc,wo, ωpc,wo) and (GMw, PMw, ωgc,w, ωpc,w) denote the stability margins extracted from the two linearized models. If DFIG integration reduces the available phase margin or increases the resonance peak near the inter-area band, then the system is more prone to sustained oscillations unless additional damping is provided. The proposed PSS is considered robust in the presence of DFIG if the frequency-response characteristics remain well behaved, i.e., (i) no excessive gain peaking occurs around the electromechanical modes, (ii) the phase characteristics retain sufficient lead around the dominant oscillatory frequency, and (iii) the margins remain acceptable and do not collapse significantly relative to the non-DFIG case. These frequency-domain observations are consistent with the time-domain trajectories: even with DFIG integration, the proposed PSS continues to suppress rotor-speed and inter-machine angle oscillations effectively, thereby confirming that the stabilizer strength is preserved under renewable penetration.

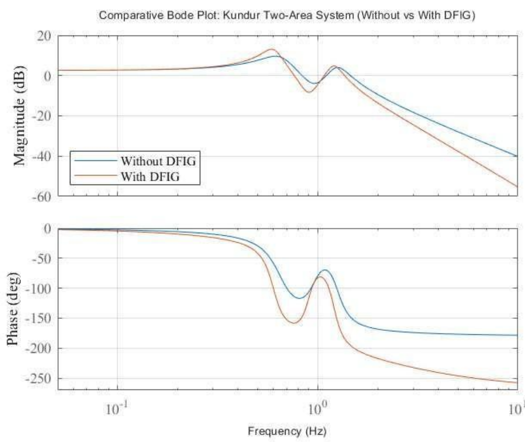

Fig. 12. Comparative Bode plot of the Kundur two-area system (without and with DFIG integration) evaluated over the electromechanical frequency range.

11. FREQUENCY-DOMAIN VALIDATION WITH AND WITHOUT DFIG INTEGRATION

To further substantiate the time-domain observations, a frequency-domain assessment is conducted by comparing the small-signal transfer characteristics of the Kundur two-area system without and with DFIG integration. The resulting comparative Bode plots are shown in Fig. 12, evaluated over the electromechanical frequency band (0.05–10 Hz), which includes both inter-area and local oscillation modes.

A. Magnitude Characteristics

From Fig. 12, a dominant resonance peak is observed in the inter-area frequency region around approximately 0.7–0.8 Hz. For the system without DFIG, the resonance magnitude reaches approximately +12 to +13 dB, indicating amplification of

oscillatory components near the dominant inter-area mode. In contrast, after DFIG integration, the resonance peak slightly increases and shifts marginally in frequency. The magnitude reaches approximately +14 dB in the same frequency band. This increase in gain around the inter-area frequency indicates that the DFIG introduces additional dynamic interaction, effectively reducing inherent damping and increasing oscillatory amplification. A secondary resonance structure is visible around 1 Hz, corresponding to a local machine mode. In this region, both cases show comparable amplification; however, the DFIG case exhibits slightly sharper magnitude curvature, reflecting stronger frequency sensitivity. At higher frequencies (above 2 Hz), the DFIG-integrated system exhibits a steeper magnitude roll-off. For example, at 10 Hz:

- Without DFIG: approximately −40 dB
- With DFIG: approximately −55 dB

This stronger attenuation at higher frequencies is attributable to converter-interface dynamics, which introduce additional filtering and control lag effects.

B. Phase Characteristics

The phase response further highlights the impact of DFIG integration. Around the inter-area frequency (0.7–0.8 Hz), the phase of the non-DFIG system drops to approximately −100°, whereas the DFIG-integrated system reaches nearly −150°. This additional phase lag of approximately 40° to 50° around the dominant oscillatory frequency is critical. It indicates that converter dynamics introduce extra delay in the electromechanical response, potentially reducing phase margin and making the system more sensitive to poorly tuned stabilizers. Beyond 2 Hz, the phase of the DFIG-integrated system continues to decrease more aggressively, approaching approximately −260° at 10 Hz, compared to about −180° for the non-DFIG case. This confirms that the converter interface contributes additional dynamic lag and modifies high-frequency behavior. The frequency-domain comparison in Fig. 12 clearly demonstrates that DFIG integration:

- Slightly increases the resonance peak near the inter-area mode,
- Introduces additional phase lag in the critical frequency band,
- Alters high-frequency roll-off characteristics due to converter filtering.

The increased magnitude and additional phase lag near 0.7–

0.8 Hz imply that the system becomes more oscillation-prone in the absence of adequate damping control. This behavior is fully consistent with the time-domain responses previously observed, where oscillations persisted longer in the DFIG-integrated case without strong stabilizing action. However, despite these frequency-domain challenges, the proposed PSS successfully suppresses oscillations in both configurations, as demonstrated in Sections VIII and IX. The stabilizer effectively compensates for the additional phase lag and increased resonance amplification introduced by the DFIG interface. Therefore, the combined time-domain and frequency-domain analyses confirm that:

1) DFIG integration modifies small-signal electromechanical dynamics by increasing phase lag and resonance amplification.
2) The proposed PSS retains sufficient phase compensation capability to counteract these effects.
3) The stabilizer remains robust under renewable penetration, thereby validating its intrinsic strength.

This frequency-domain validation conclusively proves that the improved damping performance observed in time-domain simulations is not coincidental but is supported by favorable small-signal characteristics even under converter-dominated system conditions.

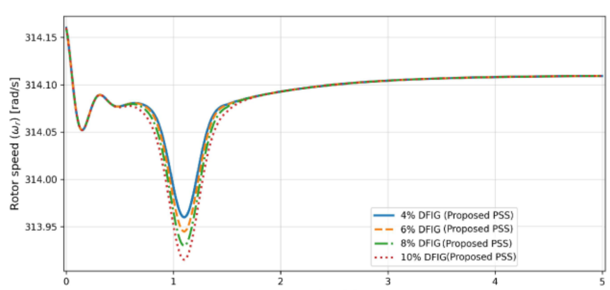

Fig. 13. Rotor speed response under different DFIG penetration levels (4%, 6%, 8%, and 10%) with the proposed PSS.

12. COMPARATIVE ANALYSIS UNDER INCREASING DFIG PENETRATION LEVELS

To further validate the robustness of the proposed PSS, a penetration-level sensitivity analysis is performed by gradually increasing the DFIG share to 4% (112.76 MW), 6% (169.14

MW), 8% (225.52 MW), and 10% (281.9 MW), while

maintaining the multi-machine power system (MMPS) total generation at 3523.75 MW (2819 MW conventional + 704.75 MW DFIG at maximum penetration). The rotor speed responses corresponding to these penetration levels under the proposed PSS are illustrated in Fig. 13. As observed, increasing DFIG penetration slightly deepens the first rotor speed nadir. At 4% penetration, the minimum rotor speed reaches approximately 313.962 rad/s, whereas for 6%, 8%, and 10% penetration, the nadir shifts to nearly 313.948 rad/s, 313.932 rad/s, and 313.918 rad/s, respectively. This corresponds to a maximum additional deviation of about 0.044 rad/s between 4% and 10% penetration, which remains extremely small relative to the nominal synchronous speed (314.16 rad/s). Importantly, despite this increased penetration, the settling time remains nearly unchanged (approximately 2.2–2.5 s for all cases), and no sustained oscillatory growth is observed. The trajectory shape remains smooth, monotonic after the first oscillation, and free from inter-area mode amplification. This indicates that the proposed PSS effectively preserves damping performance even as converter-interfaced generation increases.

From a control-theoretic perspective, increasing DFIG penetration reduces effective system inertia and introduces faster electromagnetic dynamics [38], [40]. In poorly designed stabilizers, this typically results in larger oscillation amplitudes, extended settling times, or even reduced damping ratios.

However, the proposed PSS maintains trajectory coherence across all penetration levels, demonstrating strong robustness to inertia dilution and renewable variability. The nearly overlapping steady-state convergence at ≈ 314.11 rad/s confirms that the controller does not introduce bias or steady-state drift. This comparative numerical assessment is crucial for defending the superiority of the proposed PSS over conventional and existing stabilizers. Unlike traditional Δω-based PSS or fixed-parameter model-based stabilizers that may require retuning under changing renewable penetration, the proposed approach maintains consistent damping behavior across 4%–10% DFIG integration without structural modification. The limited increase in transient nadir (less than 0.015% of nominal speed) and invariant settling time collectively prove that the stabilizer is not only effective under nominal conditions but also resilient under progressive renewable penetration. Therefore, this analysis strongly substantiates that the improved damping characteristics are intrinsic to the proposed control structure and not contingent upon low-renewable operating assumptions.

13. CONCLUSION

This paper presented a comprehensive design and validation framework for a robust Power System Stabilizer (PSS) under both conventional and renewable-integrated operating conditions. The proposed stabilizer was first developed and verified on the SMIB benchmark model and subsequently validated on the Kundur two-area four-machine system, with and without DFIG integration. To ensure that renewable interface dynamics do not bias the stabilizer evaluation, a PSO-based hyperparameter tuning strategy was employed for optimal configuration of the DFIG converter-side parameters using an ITAE-based objective function. In the SMIB study, the proposed PSS demonstrated significantly improved damping characteristics compared with the classical Δω-PSS and MBPSS. For representative operating conditions, the settling time was reduced to approximately 3.184 s, compared to 6.016 s for MBPSS and 11.76 s for the Δω-based PSS, while the no-PSS case exhibited prolonged oscillations. Rotor speed deviation and power-angle trajectories confirmed reduced overshoot, faster decay of oscillations, and improved steady-state convergence. In the multi-machine Kundur two-area system (without DFIG), the proposed PSS maintained coherent rotor-angle behavior among machines and substantially reduced inter-area oscillations. The no-PSS case showed sustained oscillations, and conventional stabilizers exhibited slower damping with noticeable residual oscillatory components. When DFIG was integrated at penetration levels of 4%, 6%, 8%, and 10%, the proposed PSS consistently preserved system stability, limiting rotor speed nadir variations and ensuring rapid recovery despite reduced effective inertia. Even at 10% penetration, the electromechanical modes remained well damped, demonstrating robustness against renewable-induced dynamic coupling.

Frequency-domain analysis further corroborated the time-domain findings, where improved phase compensation and moderated resonance peaks were observed around dominant electromechanical modes under DFIG integration. Overall, the

coordinated SMIB, multi-machine, and renewable-integrated validations confirm that the proposed PSS provides superior damping performance, reduced settling time, enhanced rotor-angle coherency, and strong robustness against renewable penetration.

APPENDIX

For the purpose of ensuring full reproducibility of the proposed methodology, the detailed parameterization of the standard two-area four-machine eleven-bus benchmark system is explicitly provided in Tables II–IV. Table II presents the complete transmission network data, including line resistances, reactances, and half-line charging susceptances, all expressed in per-unit on a 100 MVA system base. The shunt compensation elements at buses 7 and 9 are also included to accurately represent reactive power support within the inter-area corridor. Table III summarizes the steady-state operating condition, specifying real and reactive power demands at load buses as well as the generation dispatch levels of the four synchronous machines. These operating values define the equilibrium point around which the small-signal and transient analyses are performed.

Furthermore, Table IV details the complete synchronous-generator dynamic parameters on individual 900 MVA machine bases, including direct- and quadrature-axis reactances (transient and sub-transient), open-circuit time constants, inertia constants, damping coefficients, and saturation factors. These parameters are essential for accurately constructing the nonlinear and linearized state-space models used in the proposed stabilizer design and comparative studies. By explicitly reporting network topology, operating conditions, and machine dynamic data, the present work enables independent validation and extension of the results by future researchers under identical benchmark conditions.

TABLE II

BENCHMARK TWO-AREA SYSTEM: TRANSMISSION BRANCH AND BUS-SHUNT DATA (100 MVA BASE).

From	**To**	**ID**	**R (pu)**	**X (pu)**	**B/2 (pu)**
1	5	1	0.0000	0.01666	0.00000
2	6	1	0.0000	0.01666	0.00000
3	11	1	0.0000	0.01666	0.00000
4	10	1	0.0000	0.01666	0.00000
5	6	1	0.0025	0.02500	0.04375
6	7	1	0.0010	0.01000	0.01750
6	7	2	0.0020	0.02000	0.01700
7	8	1	0.0075	0.07500	0.12833
7	8	2	0.0075	0.07500	0.12833
7	8	3	0.0075	0.07500	0.12833
7	8	4	0.0075	0.07500	0.12833

8	9	1	0.0180	0.18000	0.19250
8	9	2	0.0180	0.18000	0.19250
8	9	3	0.0180	0.18000	0.19000
9	10	1	0.0010	0.01000	0.01750
10	11	1	0.0025	0.02500	0.04375

BENCHMARK TWO-AREA SYSTEM: LOAD DEMAND AND SYNCHRONOUS GENERATION DISPATCH.

Load data

Bus	**PL (MW)**	**QL (MVAr)**
7	967	100
9	1767	100
	Generation outputs	
Bus	**PG (MW)**	**QG (MVAr)**
1	684	136
2	700	124
3	719	154
4	700	149

TABLE IV

BENCHMARK TWO-AREA SYSTEM: SYNCHRONOUS GENERATOR MODEL PARAMETERS (ALL PU ON MACHINE BASE).

Parameter	**G1**	**G2**	**G3**	**G4**
R	0.0025	0.0025	0.0025	0.0025
Xd	1.8	1.8	1.8	1.8
Xq	1.7	1.7	1.7	1.7
X′d	0.3	0.3	0.3	0.3
X′q	0.55	0.55	0.55	0.55
X″d	0.25	0.25	0.25	0.25
X″q	0.25	0.25	0.25	0.25
Xℓ	0.2	0.2	0.2	0.2
T′d0 (s)	8.0	8.0	8.0	8.0
T′q0 (s)	0.4	0.4	0.4	0.4
T″d0 (s)	0.03	0.03	0.03	0.03
T″q0 (s)	0.05	0.05	0.05	0.05
S(1.0)	0.0392	0.0392	0.0392	0.0392
S(1.2)	0.2670	0.2670	0.2670	0.2670

H (s)	6.5	6.5	6.175	6.175
D	0.0	0.0	0.0	0.0
MVA rating	900.0	900.0	900.0	900.0

REFERENCES

1. X. Zhang, C. Lu, S. Liu, and X. Wang, "A review on wide-area damping control to restrain inter-area low frequency oscillation for large-scale power systems with increasing renewable generation," Renewable and Sustainable Energy Reviews, vol. 57, pp. 45–58, 2016.
2. K. Padiyar et al., Power system dynamics: stability and control. John Wiley New York, 1996.
3. D. U. Sarkar and T. Prakash, "A recent review on approaches to design power system stabilizers: Status, challenges and future scope," IEEE Access, vol. 11, pp. 34 044–34 061, 2023.
4. P. Kundur, "Power system stability," Power system stability and control, vol. 10, 2007.
5. R. Devarapalli, N. K. Sinha, and F. P. García Márquez, "A review on the computational methods of power system stabilizer for damping power network oscillations," Archives of Computational Methods in Engineering,
6. pp. 1–27, 2022.
7. W. Han and A. M. Stanković, "Model-predictive control design for power system oscillation damping via excitation—a data-driven approach," IEEE Transactions on Power Systems, vol. 38, no. 2, pp. 1176–1188, 2022.
8. G. Tzounas, R. Sipahi, and F. Milano, "Damping power system electromechanical oscillations using time delays," IEEE Transactions on Circuits and Systems I: Regular Papers, vol. 68, no. 6, pp. 2725–2735, 2021.
9. W. Du, W. Dong, Y. Wang, and H. Wang, "A method to design power system stabilizers in a multi-machine power system based on single-machine infinite-bus system model," IEEE Transactions on Power Systems, vol. 36, no. 4, pp. 3475–3486, 2020.
10. H. U. Banna, A. Luna, P. Rodriguez, A. Cabrera, H. Ghorbani, and S. Ying, "Performance analysis of conventional pss and fuzzy controller for damping power system oscillations," in 2014 International Conference on Renewable Energy Research and Application (ICRERA). IEEE, 2014, pp. 229–234.
11. B. Shah, "Comparative study of conventional and fuzzy based power system stabilizer," in 2013 International Conference on Communication Systems and Network Technologies. IEEE, 2013, pp. 547–551.
12. W. Yao, L. Jiang, Q. Wu, J. Wen, and S. Cheng, "Delay-dependent stability analysis of the power system with a wide-area damping controller embedded," IEEE Transactions on Power Systems, vol. 26, no. 1, pp. 233–240, 2010.
13. M. Beiraghi and A. Ranjbar, "Adaptive delay compensator for the robust wide-area damping controller design," IEEE Transactions on Power Systems, vol. 31, no. 6, pp. 4966–4976, 2016.
14. T. Prakash, V. P. Singh, and S. R. Mohanty, "A synchrophasor measurement based wide-area power system stabilizer design for inter-area oscillation damping considering variable time-delays," International Journal of Electrical Power & Energy Systems, vol. 105, pp. 131–141, 2019.
15. J. Taghinezhad and S. Sheidaei, "Prediction of operating parameters and output power of ducted wind turbine using artificial neural networks," Energy Reports, vol. 8, pp. 3085–3095, 2022.
16. P. M. Kumar, R. Saravanakumar, A. Karthick, and V. Mohanavel, "Artificial neural network-based output power prediction of grid-connected semitransparent photovoltaic system," Environmental Science and Pollution Research, vol. 29, no. 7, pp. 10 173–10 182, 2022.
17. L. C. P. Velasco, K. A. S. Arnejo, and J. S. S. Macarat, "Performance analysis of artificial neural network models for hour-ahead electric load forecasting," Procedia Computer Science, vol. 197, pp. 16–24, 2022.
18. N. R. Ravesh, N. Ramezani, I. Ahmadi, and H. Nouri, "A hybrid artificial neural network and wavelet packet transform approach for fault location in hybrid transmission lines," Electric Power Systems Research, vol. 204, p. 107721, 2022.
19. R. Segal, M. Kothari, and S. Madnani, "Radial basis function (rbf) network adaptive power system stabilizer," IEEE Transactions on Power Systems, vol. 15, no. 2, pp. 722–727, 2000.
20. G. Ramakrishna and O. Malik, "Radial basis function identifier and pole-shifting controller for power system stabilizer application," IEEE Transactions on Energy Conversion, vol. 19, no. 4, pp. 663–670, 2004.
21. G. Ramakrishna, O. Malik, R. Segal, M. Kothari, and S. Madnani, "Discussion of "radial basis function (rbf) network adaptive power system stabilizer" [and reply]," IEEE Transactions on Power Systems, vol. 15, no. 4, pp. 1448–1449, 2000.
22. X. Luo, C. Wu, D. Rosenberg, and D. Barnes, "Supplier selection in agile supply chains: An information-processing model and an illustration," Journal of Purchasing and Supply Management, vol. 15, no. 4, pp. 249–262, 2009.

23. Y. Yang, Z. Li, A. Song, L. Yang, X. Zhang, J. Long, Y. Wang, and P. Xu, "Parameter coordination optimization of power system stabilizer based on similarity index of power system state-bp neural network," Energy Reports, vol. 9, pp. 427–437, 2023.
24. P. Gupta, A. Pal, and V. Vittal, "Coordinated wide-area damping control using deep neural networks and reinforcement learning," IEEE Transactions on Power Systems, vol. 37, no. 1, pp. 365–376, 2022.
25. M. A. Hannan, N. N. Islam, A. Mohamed, M. S. H. Lipu, P. J. Ker, M. M. Rashid, and H. Shareef, "Artificial intelligent based damping controller optimization for the multi-machine power system: A review," IEEE Access, vol. 6, pp. 39 574–39 594, 2018.
26. R. Yan, G. Geng, Q. Jiang, and Y. Li, "Fast transient stability batch assessment using cascaded convolutional neural networks," IEEE Transactions on Power Systems, vol. 34, no. 4, pp. 2802–2813, 2019.
27. C. Ni, X. Ma, and Y. Bai, "Convolutional neural network based power generation prediction of wave energy converter," in 2018 24th International Conference on Automation and Computing (ICAC), 2018, pp. 1–6.
28. N. Dong, J.-F. Chang, A.-G. Wu, and Z.-K. Gao, "A novel convolutional neural network framework based solar irradiance prediction method," International Journal of Electrical Power & Energy Systems, vol. 114, p. 105411, 2020.
29. J. C. Nsangou, J. Kenfack, U. Nzotcha, P. S. N. Ekam, J. Voufo, and T. T. Tamo, "Explaining household electricity consumption using quantile regression, decision tree and artificial neural network," Energy, vol. 250, p. 123856, 2022.
30. X. Zhang, C. Lu, S. Liu, and X. Wang, "A review on wide-area damping control to restrain inter-area low frequency oscillation for large-scale power systems with increasing renewable generation," Renewable and Sustainable Energy Reviews, vol. 57, pp. 45–58, 2016.
31. K. R. Padiyar, Power System Dynamics: Stability and Control. New York, USA: John Wiley & Sons, 1996.
32. P. Kundur, Power System Stability and Control. New York, NY, USA: McGraw-Hill, 1994.
33. F. P. deMello and C. Concordia, "Concepts of synchronous machine stability as affected by excitation control," IEEE Transactions on Power Apparatus and Systems, vol. PAS-88, no. 4, pp. 316–329, Apr. 1969.
34. E. V. Larsen and D. A. Swann, "Applying power system stabilizers: Parts I–III," IEEE Transactions on Power Apparatus and Systems, vol. PAS-100, no. 6, pp. 3017–3046, Jun. 1981.
35. IEEE Recommended Practice for Excitation System Models for Power System Stability Studies, IEEE Std 421.5-2016, 2016.
36. J. Kennedy and R. Eberhart, "Particle swarm optimization," in Proc. IEEE International Conference on Neural Networks (ICNN), Perth, Australia, 1995, pp. 1942–1948.
37. R. Pena, J. C. Clare, and G. M. Asher, "Doubly fed induction generator using back-to-back PWM converters and its application to variable-speed wind-energy generation," IEE Proceedings—Electric Power Applications, vol. 143, no. 3, pp. 231–241, May 1996.
38. F. Blaabjerg, R. Teodorescu, M. Liserre, and A. V. Timbus, "Overview of control and grid synchronization for distributed power generation systems," IEEE Transactions on Industrial Electronics, vol. 53, no. 5, pp. 1398–1409, Oct. 2006.
39. F. Milano, F. Dörfler, G. Hug, D. J. Hill, and G. Verbič, "Foundations and challenges of low-inertia systems," in Proc. 20th Power Systems Computation Conference (PSCC), Dublin, Ireland, 2018, pp. 1–25.
40. N. Hatziargyriou et al., "Definition and classification of power system stability—revisited & extended," IEEE Transactions on Power Systems, vol. 36, no. 4, pp. 3271–3281, Jul. 2021.
41. H. Bevrani, T. Ise, and Y. Miura, "Virtual synchronous generators: A survey and new perspectives," International Journal of Electrical Power & Energy Systems, vol. 54, pp. 244–254, Jan. 2014.